atmosphere

Article

Projected Changes in Urban Impacts on Summer Mean Temperature and Precipitation over Eastern North America

Jangsoo Kim [1] and Seok-Geun Oh [2,*]

[1] Institute of Regional Development Research, Kongju National University, Gongju-si 32588, Republic of Korea; matra99@kongju.ac.kr
[2] School of Earth and Environmental Sciences, Seoul National University, Seoul 08825, Republic of Korea
[*] Correspondence: seokgeunoh@snu.ac.kr

Abstract

Urban–climate interactions in a warming climate remain largely uncertain; therefore, it is crucial to realistically evaluate and project these feedbacks to establish effective adaptation strategies. This study investigates projected shifts in summertime urban–climate interactions over eastern North America by employing the GEM regional climate model coupled with the Town Energy Balance (TEB) scheme, driven by RCP4.5 and RCP8.5 scenarios for the 1981–2100 period. Evaluations for the current climate (1981–2010) demonstrate that the model simulates an urban-induced warming of 0.5–0.7 °C and a precipitation reduction of 0.2–0.4 mm/day with high fidelity. By the late 21st century (2071–2100), projections under the RCP8.5 scenario indicate a steady weakening of the summer mean Urban Heat Island (UHI) intensity by approximately 0.10 °C, with a more pronounced nighttime attenuation of 0.15 °C. Physically, this weakening is attributed to an enhanced urban-induced evaporative fraction, which limits solar radiation storage within the urban fabric during the day, thereby reducing the thermal energy available for post-sunset release. This UHI attenuation correlates strongly with localized increases in precipitation, particularly in coastal regions where urban-induced effects contribute 20–40% to the total precipitation rise. While this study intentionally utilizes static urban boundaries to isolate the specific sensitivities of current urban morphologies to global warming, these results emphasize that diverse climatological regions will undergo distinct urban–climate feedback changes, providing essential baseline data for resilient urban planning.

Keywords: urban–climate interaction; regional climate model; RCP scenarios; North America

1. Introduction

Rapid urbanization in recent decades has strongly modified social and environmental conditions and in particular can bring out more extreme temperature and precipitation events [1–4]. Considering the fact that today 55% of the entire world's population lives in urban regions and the percentage is projected to increase to 68% by 2050 [5], this means that humans may be more extensively exposed to the hazards resulting from severe weather and climate extremes in urban areas. In particular, the role of urban–climate interactions in a warming climate remains largely uncertain; therefore, realistically evaluating and projecting urban–climate interactions for both current and future climates is crucial for establishing effective adaptation and mitigation strategies against anthropogenic warming (e.g., greenhouse gas-induced warming and the Urban Heat Island effect).

Academic Editor: Teodoro Georgiadis

Received: 18 March 2026
Revised: 18 April 2026
Accepted: 23 April 2026
Published: 26 April 2026

Global climate model-based studies have been conducted to evaluate the changes in relative effects in UHI effects under the greenhouse gas-induced warming climate (e.g., [6–9]). For example, Oleson [8] in his study of using a new parameterization of urban areas in the Community Climate System Model version 4 (CCSM4), reported that the globally averaged UHI, defined as the simulated urban minus rural air temperature, at the end of the 21st century is similar to that of the current climate under Representative Concentration Pathway (RCP) 2.6 and 4.5 scenarios but decreases in RCP8.5. These UHI decreases of around 0.13 °C and 0.08 °C are simulated, respectively, during daytime and nighttime, and the daytime UHI decrease is mainly associated with the changes in evaporation for urban and non-urban/rural regions. They, therefore, suggested that the distinct characteristics of the urban region must be accounted for when developing climate change projection, as urban and non-urban/rural regions respond differently to climate change.

A good alternative approach for simulating urban–climate interactions is the employment of regional climate models, which facilitate high-resolution modeling of atmospheric and land surface fields (e.g., [2,10–12]). Recently, the integration of regional climate dynamic downscaling with advanced urban surface parameterizations has emerged as a highly effective approach for climate studies. This coupled framework enables a realistic representation of regional-scale thermodynamic and hydrological impacts across diverse urban surfaces—such as roofs, walls, and roads—without the computational necessity of explicitly resolving micro-scale canyon dynamics [1,2,13]. The horizontal resolution of 0.22° (approximately 25 km) adopted in this study is consistent with established regional climate downscaling initiatives, such as CORDEX, and is optimally designed to capture mesoscale processes and land–atmosphere interactions while maintaining the feasibility of long-term climate simulations. Accordingly, the primary methodological strength of this research lies in the synergy between dynamic downscaling and physically based urban parameterization. This integrated approach ensures a physically consistent representation of regional urban-climate feedbacks, providing a robust foundation for assessing future urban–climate interactions. Bélair et al. [13] and Daniel et al. [1] proved the enhanced performance of the regional climate model integrated with the advanced urban canopy parameterization in reproducing extreme precipitation through the enhanced lateral inflow of moist static energy in Tokyo, Japan, and the diurnal variation of 2 m surface temperature in Paris, France, respectively. Oh and Sushama [2] in their study assessing urban–climate interactions during the summer for eastern North America spanning 1981 to 2010, utilizing paired regional climate model simulations with and without an urban canopy parameterization, reported that the realistically simulated higher urban temperature can contribute to strengthening thermal and dynamic convections, which result in more hourly precipitation extremes for high-temperature bins, particularly for coastal and Great Lakes urban regions. In addition, they demonstrate the difference in urban–climate feedbacks across distinct climatic zones, which suggests the necessity of improved urban parameterization in regional climate models to produce reliable climate projections.

While previous regional modeling efforts have successfully demonstrated the added value of urban parameterizations in present-day climates (e.g., [2]), the transient response of urban–climate feedbacks under sustained greenhouse gas forcing remains largely unexplored at the regional scale. Therefore, the purpose of this study is to systematically assess how projected shifts in background climate alter summertime urban–climate interactions over eastern North America across diverse emission scenarios. By isolating the specific sensitivities of urban morphologies to varying degrees of global warming, this study will provide crucial baseline data to support climate-resilient urban planning, particularly in anticipating non-linear shifts in the urban hydrological cycle and localized heat stress.

The remainder of this paper is organized as follows. Section 2 briefly outlines the regional climate model, the urban canopy parameterization, and the experimental framework applied in this research. Section 3 presents an evaluation of the performance of paired regional climate simulations—both incorporating and excluding the urban canopy parameterization—for the current climate compared to observations, thereby assessing the enhanced performance of the integrated modeling approach. Based on this, projected changes to urban–climate interactions for the future climate compared to the current climate are assessed. The summary and conclusion are presented in Section 4.

2. Model and Experimental Design

2.1. Regional Climate Model

The regional climate model used in this study is the limited-area version of the Global Environmental Multiscale (GEM) model, developed by Environment and Climate Change Canada (ECCC) [14,15]. The GEM model employs a non-hydrostatic dynamical core, an Arakawa C-grid staggering in the horizontal, and a hybrid terrain-following vertical coordinate system. It employs a two-time-level semi-Lagrangian implicit scheme. Consistent with Oh and Sushama [2], this study employs the deep convection parameterization of Kain and Fritsch [16], the shallow convection scheme of Bélair et al. [17], and the resolvable large-scale precipitation scheme of Sundqvist et al. [18]. Solar and terrestrial radiation are computed using the correlated-k parameterization [19]. The model employs the planetary boundary layer parameterization developed by Benoit et al. [20] and Delage [21], incorporating modifications by Zadra et al. [22]. The Canadian Land Surface Scheme (CLASS, version 3.5) [23], which has been used and evaluated in many previous studies (e.g., [12]), is used as the land surface parameterization. In this study, CLASS is configured with 26 levels reaching a total depth of 10 m. In CLASS, the thermal budget is computed for all soil layers, while the hydrological budget is restricted to layers above the bedrock. For urban–climate interactions, urban regions are treated as bare soil with reduced permeability within the scheme. Therefore, we use the Town Energy Balance (TEB) [24,25] scheme, which is based on the mean urban canyon approach [26], to simulate urban–climate interactions with high fidelity. The TEB scheme is composed of elementary urban surfaces, such as roofs, roads, and walls. Accordingly, the scheme utilizes averaged geometric parameters—such as building height, density, and street aspect ratio—alongside mean thermal and radiative properties. The temporal evolution of roof, wall, and road temperatures is prognostically calculated through individual surface energy budgets, including conductive heat transfer. Several studies have employed the GEM model coupled with the TEB scheme [2,13], demonstrating its enhanced performance in simulating urban climates. More comprehensive details of the TEB parameterization can be found in Masson [24] and Masson et al. [25]. Furthermore, to represent lakes, the model incorporates the one-dimensional FLake model [27].

2.2. Experimental Design and Methodology

The experimental design of this study follows the framework established by Oh and Sushama [2]. The model domain covers eastern North America and its adjacent oceans (Figure 1), consisting of 145 × 148 grid points at a 0.22° spatial resolution (~25 km) with 62 vertical levels. While this resolution is relatively coarse for resolving micro-scale canyon dynamics, it has proven sufficient for capturing the regional-scale thermodynamic and hydrological impacts induced by urban parameterizations. To isolate the specific feedback mechanisms associated with urban coupling, this study employs a highly controlled, process-oriented sensitivity analysis based on the CanESM2–GEM modeling chain. Rather than providing probabilistic projections, this single-chain approach is designed to avoid compounding structural uncertainties inherent in multi-model ensembles, thereby allowing for a clearer isolation of the thermodynamic and hydrological responses strictly driven by urban processes. The GEM regional climate model provides a robust, well-established framework for urban simulations through its coupling with the Town Energy Balance (TEB) scheme, demonstrating high fidelity in capturing 2 m surface climate responses [2,13]. As the driving global model, CanESM2 ensures superior dynamical consistency with the GEM framework, given its extensively evaluated capacity to realistically reproduce large-scale atmospheric circulation and boundary forcings over the study region [27,28]. The simulations are driven by the Representative Concentration Pathway (RCP) 4.5 and 8.5 scenarios, maintaining strict dynamical consistency with the CMIP5-generation CanESM2 forcings. Transitioning to different driving global models solely to incorporate Shared Socioeconomic Pathway (SSP) scenarios would introduce structural deviations that could obscure the targeted interpretation of urban–climate feedbacks. Furthermore, the large-scale radiative forcing trajectories of RCP4.5 and RCP8.5 remain physically robust and are widely recognized as comparable to those of SSP2-4.5 and SSP5-8.5, respectively [29,30]. Because this study focuses on urban-induced relative changes under comparable warming conditions, these thermodynamic forcings provide a valid and scientifically robust baseline. Ultimately, this single-model framework minimizes inter-model spread, offering a highly controlled environment to identify specific physical mechanisms prior to broader multi-model ensemble assessments [31]. The added value of dynamic downscaling (discussed in Section 3.1) partially mitigates the coarse-resolution biases inherent in the driving CanESM2 data. Two experiments, with and without the TEB scheme, are performed to investigate urban–climate interactions over the model domain for the 1981–2100 period driven by RCP4.5 and RCP8.5 [32] scenarios starting from 2006. The choice of RCP scenarios ensures consistency with previous studies (e.g., [2]). Furthermore, because RCP4.5 and RCP8.5 share analogous end-of-century radiative forcing targets with SSP2-4.5 and SSP5-8.5, respectively, the fundamental physical mechanisms and urban–climate feedbacks identified in this study remain highly relevant to interpreting contemporary CMIP6 projections. The simulations with and without the TEB scheme will be named as GEM_TEB and GEM, respectively, and in this study, we consider the difference between GEM_TEB and GEM (GEM_TEB minus GEM) as urban impacts. For representing realistic urban characteristics in the GEM_TEB experiment, the pavement and building fractions are specified using recent information from OpenStreetMap [13]; the urban fraction is presented in Figure 1 as the sum of the above two variables. For the GEM_TEB experiment, TEB-specific urban parameters such as building height, canyon aspect ratio, roof (wall/road) albedo and emissivity, and roughness length, etc., are required. While maintaining fixed urban boundaries throughout the 21st century may underrepresent the total future urban heat hazard by excluding urban expansion, this idealized setup provides a controlled framework to strictly isolate the thermodynamic sensitivity of current urban morphologies to greenhouse gas forcing.

The spatial domain of this study encompasses eastern North America (Figure 1), representing a geographically coherent region characterized by a humid and precipitation-active climate regime. This domain provides a highly constrained framework for examining thermodynamic and hydrological responses to warming, as urban–climate interactions within this region are strongly governed by moisture availability, land–atmosphere coupling, and convective processes [2,33]. Moreover, the high density of major urban centers distributed across distinct yet dynamically related climate sub-regimes—including humid subtropical, continental, and Great Lakes-influenced environments—facilitates a robust comparative analysis under a relatively consistent large-scale atmospheric circulation.

To rigorously isolate the physical mechanisms driving urban–climate feedbacks, the experimental design minimizes confounding large-scale climatic variability [31]. By restricting the analysis to moisture-abundant environments, the framework precludes the convolution of distinct thermodynamic processes that dictate urban boundary layers in arid and semi-arid regimes (e.g., the western United States and Mexico) [27]. Consequently, this strictly defined spatial boundary establishes a highly controlled baseline, ensuring that the sensitivity of urban morphologies to warming is evaluated within a consistent set of humid and continental background conditions.

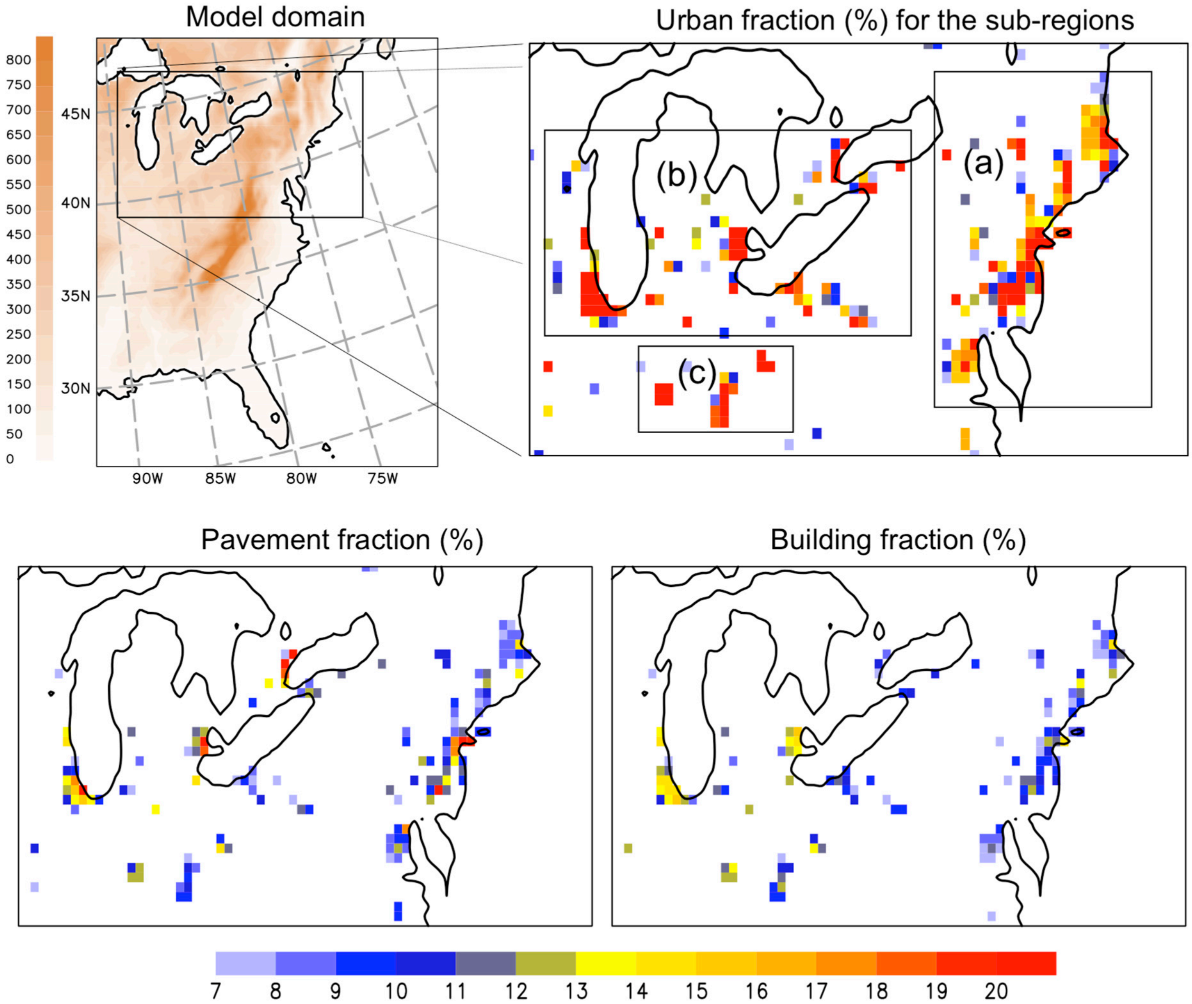

Figure 1. Model domain (excluding blending and halo zones) with topography (in m; **left panel**) at 0.22° horizontal resolution. The three sub-regions ((**a**)coastal, (**b**) Great Lakes and (**c**) inland regions) used for detailed analysis and urban fractions (in %; **upper-right panel**). The pavement and building fractions (%) over the study domain (**lower panels**).

To evaluate two model simulations and assess the added value of GEM_TEB for the current climate (1981–2010), the Daymet version 3 daily gridded dataset [34], which provides a daily temporal resolution and 1 km horizontal resolution over North America, is used for the same current period. The observed variables are interpolated to the model grid to facilitate comparison. In addition, we together use the GEM simulations with and without the TEB scheme driven by the European Centre for Medium-Range Weather Forecast (ECMWF) Re-Analysis (ERA)-Interim [35] for the current climate (1981–2010), which are used in Oh and Sushama [2], to quantify the uncertainty associated with boundary forcing data. In addition, the interpolated 2 m surface temperature and precipitation of CanESM2 to the model grid for the current climate (1981–2010) are also used to assess the added value of dynamic downscaling.

In this study, the comparison of model simulations is conducted with respect to the following processes and mechanisms: (1) comparison of spatial distribution of 2 m surface temperature and precipitation and related surface energy fluxes, and evaluation of the added value of the coupled simulation with TEB for the current climate (1981–2010), (2) time series analysis of urban impacts on the simulated 2 m surface temperature and precipitation according to RCP scenarios, and related mechanism analysis based on the correlation matrix. The simulated 2 m surface temperature and precipitation for the current climate (1981–2010) are evaluated against observations and the differences in simulated surface energy fluxes are used to explain urban-induced climate processes. In addition, a Taylor diagram is used to assess the added value of the coupled simulation with TEB for climatologically different regions [36]. In brief, in this study, fundamentally a point with a normalized standard deviation and spatial correlation coefficient of one is the reference point, which indicates perfect model performance. The distance from each model point to the reference point, therefore, indicates the model errors related to spatial patterns. To investigate the causes of changes in urban-induced surface variables for future climate, a linear relationship in the difference between projected changes in various surface variables (e.g., daily maximum and minimum temperatures, evaporation fraction, downward longwave radiation, surface wind speed, etc.) simulated by GEM_TEB minus GEM for future climate (2071–2100) compared to the current climate (1981–2010) is summarized through a correlation matrix.

3. Results

3.1. Evaluation of Urban–Climate Interactions for Current Climate

Figures 2 and 3 show the spatial distribution of observed and modeled mean summer 2 m surface temperatures (°C) and precipitation (mm/day) for the current climate (1981–2010), respectively. Taylor diagrams for 2 m surface temperature and precipitation in three sub-regions such as coastal, Great Lakes, and Inland regions are also presented to assess the added value of the coupled simulation with the TEB scheme. Notably, the Taylor diagram analysis exclusively utilizes grid cells with an urban fraction exceeding 8% for each sub-region, as depicted in Figure 1. As reported by Oh and Sushama [2], in general, GEM_TEB driven by ERA-Interim reproduces well the observed spatial patterns of 2 m surface temperature and precipitation, which shows high spatial correlations of around 0.94 and 0.61 and small biases of 0.28 °C and 0.18 mm/day, respectively. This means that GEM_TEB can realistically capture the spatial patterns of two surface variables affected by climatologically geographic locations when driven by the perfect boundary forcing data.

However, GEM_TEB driven by CanESM2 shows systematic warm and dry biases of 3.05 °C and 1.19 mm/day, respectively, for 2 m surface temperature and precipitation over the entire analysis domain compared to observations, and these systematic warm and dry biases seem to be inherited from its driving data, CanESM2 (Figures 2a and 3a). However, for 2 m surface temperature, GEM_TEB driven by CanESM2 realistically reproduces geographical features of temperature induced by the difference in latitude, land cover, and topography, compared to CanESM2, which results in an improvement in the statistics for bias (GEM_TEB: 3.05 °C, CanESM2: 4.67 °C) and spatial correlation (GEM_TEB: 0.86, CanESM2: 0.78). For precipitation, model performance varies across the regions but GEM_TEB driven by CanESM2 simulates stronger precipitation intensities for the mountainous region and coastal region compared to CanESM2, leading to improved performance compared to observations. In particular, higher spatial correlation in GEM_TEB (0.50) than CanESM2 (0.46) is found for the entire analysis domain (Figure 3a). Although the driving global model introduces systematic mean-state biases, the magnitudes of the simulated urban-induced warming (0.5–0.7 °C) and precipitation reduction (0.2–0.4 mm/day) are physically realistic and consistent with previous observational and modeling studies [1–3,37,38]. While direct station-based validation is inherently constrained by scale mismatches between point observations and regional grids, the simulated regional urban responses align well with established urban-climate dynamics [39]. Crucially, previous simulations over the identical domain driven by the ERA-Interim reanalysis—which demonstrate significantly improved baseline performance—yield analogous spatial patterns and urban-induced thermodynamic responses [2]. This consistency across independent boundary forcings confirms that the simulated urban–climate signals are physically robust and not merely artifacts of the CanESM2 biases. Therefore, the above results indicate that GEM_TEB has the added value of dynamic downscaling when compared to its driving data, CanESM2.

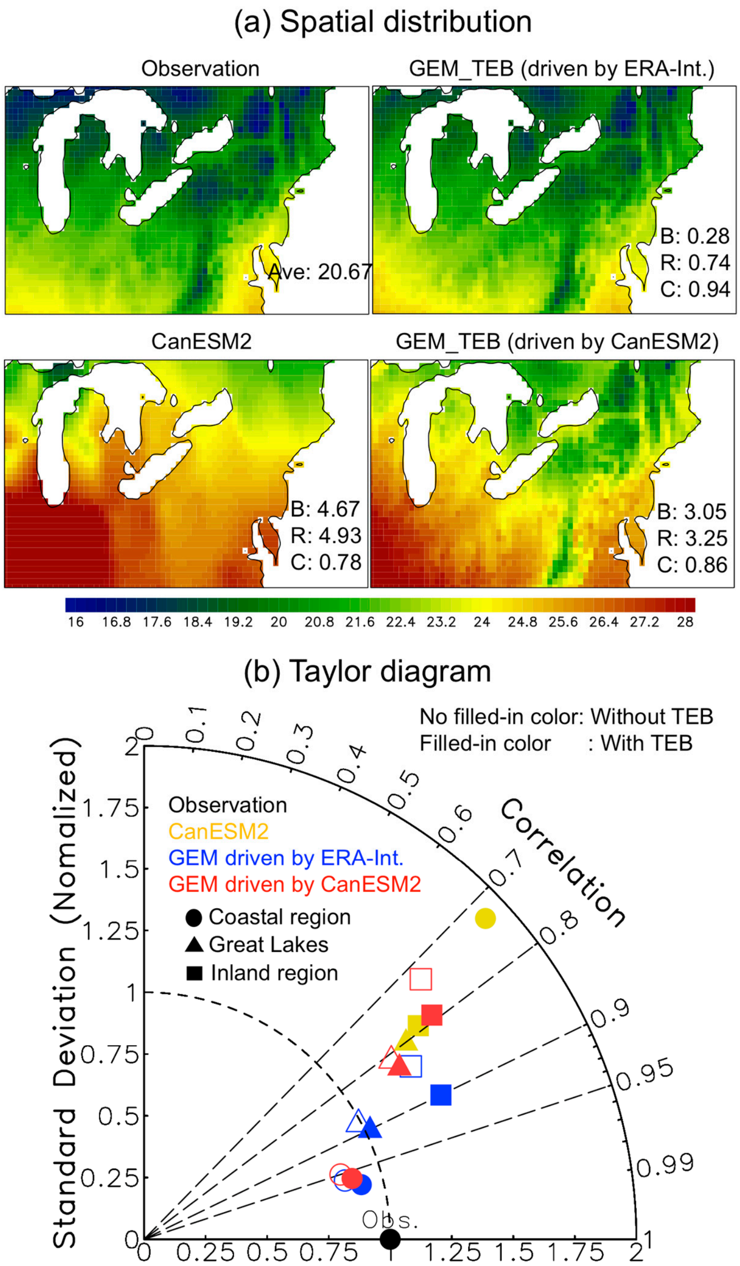

Figure 2. Performance evaluation for summer mean 2 m surface temperature (°C) during the current climate (1981–2010): (**a**) spatial distribution of observed and modeled values, including domain-wide bias (B), root mean square error (R), and spatial correlation (C); (**b**) Taylor diagrams comparing simulations with and without the TEB scheme driven by ERA-Interim and CanESM2 across three sub-regions (coastal, Great Lakes, and inland). To ensure clear identification of the multi-dimensional data points, please refer to the high-resolution version of this figure; all markers for different experiments and datasets are clearly distinguishable upon magnification.

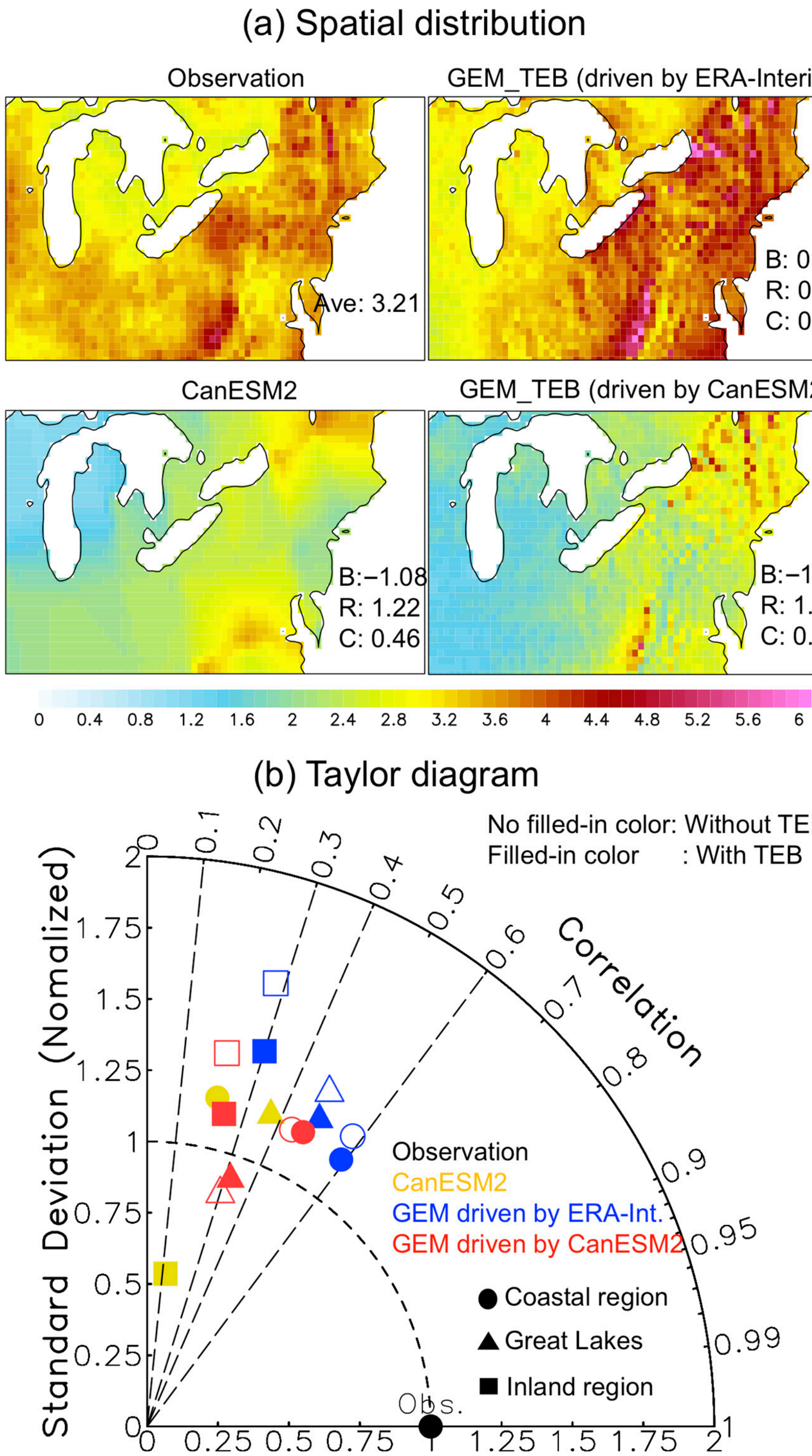

Figure 3. As in Figure 2, but for summer mean precipitation (mm/day): (**a**) spatial distribution with associated performance statistics (B, R, and C) and (**b**) Taylor diagrams across the three sub-regions for various model configurations and driving datasets. Regarding the dense symbol layout, please refer to the high-resolution version of this figure to ensure markers are clearly distinguishable upon magnification.

The Taylor diagram analysis confirms the noticeable improvement provided by dynamic downscaling for 2 m surface temperature and precipitation across all sub-regions, particularly for coastal urban grids. The comparison of 2 m surface temperature between the simulations with and without the TEB scheme suggests that GEM_TEB experiments show the improved performance for all sub-regions, irrespective of the driving datasets, compared to the GEM experiments. In particular, the spatial correlations are relatively higher by around 0.03–0.07 depending on region and driving dataset (Figure 2b). On the other hand, for precipitation, the GEM_TEB experiments also show the better performance for all sub-regions than those of the GEM experiments, irrespective of the driving dataset. Interestingly, while the spatial correlations for precipitation show only marginal gains, the normalized standard deviations are noticeably improved, moving closer to the observation-based value of one. This indicates that the inclusion of the TEB scheme significantly enhances the model's ability to reproduce the spatial variability and magnitude of urban-induced convective precipitation, even if the precise linear spatial pattern remains challenging to capture at this resolution. The above validation results, therefore, indicate that the GEM_TEB experiments improve the overall representation of climatological features for 2 m surface temperature and precipitation across urban grids compared to the GEM experiments.

Figure 4 presents the spatial distributions of summer mean differences (GEM_TEB minus GEM) for 2 m temperature, precipitation, albedo, sensible and latent heat fluxes, and 2 m specific humidity under the current climate (1981–2010). The CanESM2-driven simulations indicate that urban regions experience a statistically significant ($p < 0.05$) temperature increase of 0.5–0.7 °C and a precipitation reduction of 0.2–0.4 mm/day relative to the GEM experiment. These surface modifications directly correspond to reduced albedo (1–3%) and limited soil moisture availability within the urban canopy. Consequently, the enhanced absorption of daytime solar radiation and restricted evapotranspiration lead to a pronounced shift in surface energy partitioning, characterized by increased sensible heat flux (>16 W m^{-2}) and decreased latent heat flux (>16 W m^{-2}) in urbanized cells. The lower precipitation over urban and surrounding rural areas is thus a direct consequence of the reduced 2 m specific humidity (0.3–0.6 g kg^{-1}) driven by this latent heat flux deficit.

Importantly, the partitioning of surface energy fluxes associated with the TEB parameterization demonstrates robust physical consistency regardless of the driving boundary conditions. A comparison of these CanESM2-driven surface energy flux anomalies with those derived from ERA-Interim-driven simulations [2] reveals that the spatial structures and magnitudes are statistically comparable. This agreement indicates that the urban-induced modifications to the surface energy balance are fundamentally governed by the intrinsic physical properties of urban surfaces—such as increased imperviousness and reduced evapotranspiration—rather than by non-linear amplifications arising from the background climate state. The secondary role of large-scale atmospheric biases relative to parameterized urban processes confirms that the physical attribution of urban-induced changes remains robust. Consequently, the projected future urban impacts simulated under the CanESM2 forcing can be interpreted with high physical confidence, which is the focus of Section 3.2.

https://doi.org/10.3390/atmos17050441

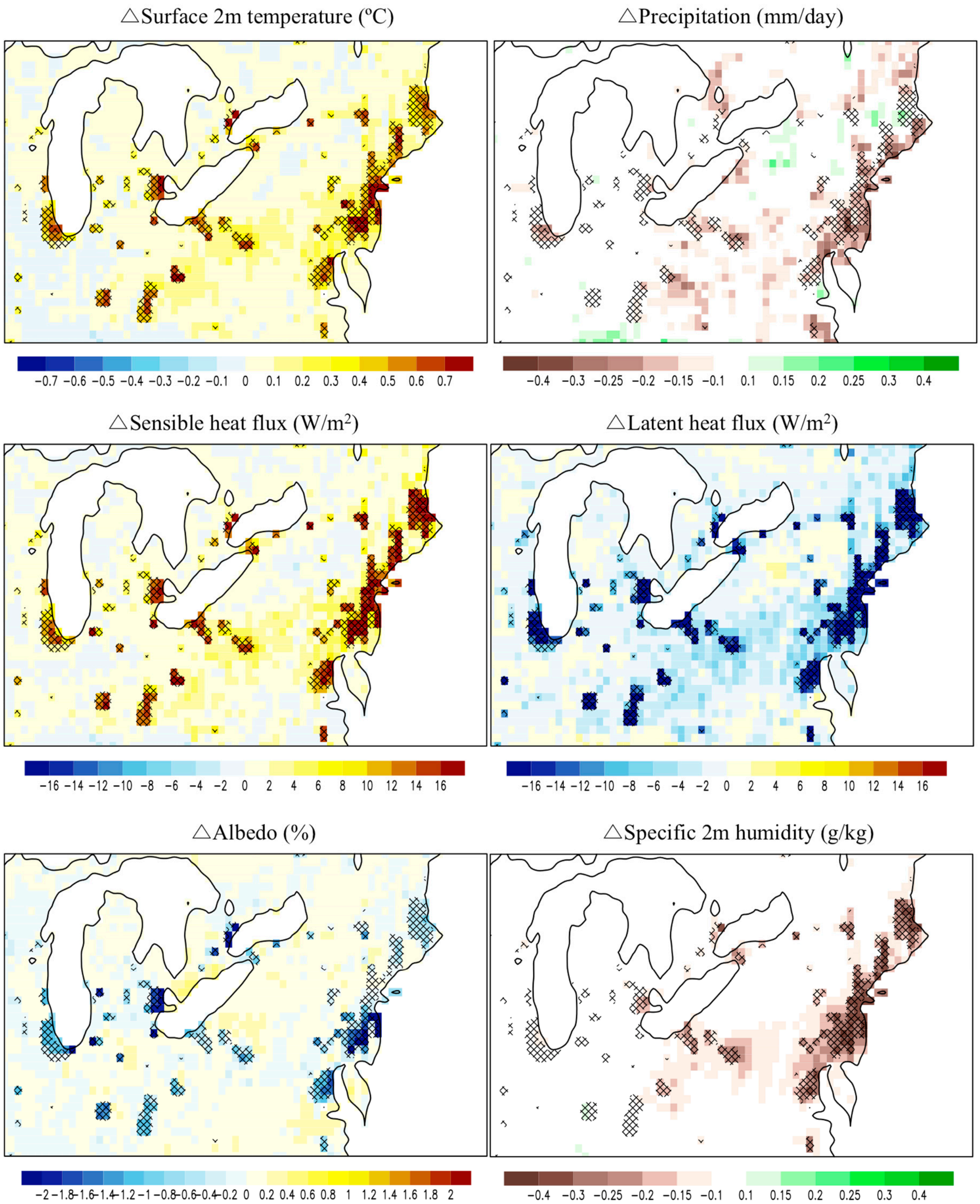

Figure 4. Spatial distribution of the differences (GEM_TEB minus GEM) in the modeled summer 2 m surface temperature (°C), precipitation (mm/day), sensible and latent heat fluxes (W/m^2), albedo (%), and 2 m surface humidity (g/kg) for current climate (1981–2010). The hatched areas indicate the urban regions. The results in these sub-figures are obtained from GEM_TEB and GEM driven by CanESM2. To ensure transparent reporting of statistical robustness, only grid cells exhibiting significant changes at the 5% significance level ($p < 0.05$), determined by a two-tailed Student's *t*-test, are color-shaded to highlight physically robust signals. Areas not meeting this threshold are masked (left blank) to avoid the misinterpretation of insignificant noise.

3.2. Projected Changes to Urban–Climate Interactions

Figure 5 shows the time series for projected changes to 2 m surface temperature (°C) and precipitation (mm/day) simulated by GEM_TEB driven by CanESM2 over all urban regions for the 2011–2100 period according to the RCP4.5 and 8.5 scenarios with respect to the current climate (1981–2010). In addition, the time series of the difference between the GEM_TEB and GEM experiments (GEM_TEB minus GEM) over all urban regions are also presented to investigate the changes in urban impacts on the two surface variables under the RCP scenarios. To reiterate, the analysis focuses exclusively on grid cells with urban fractions exceeding 8% for each sub-region, as shown in Figure 1, which are used in the analysis, and a 10-year moving average approach is applied to filter out stochastic noise from outliers and highlight decadal trends. For the time series projected by GEM_TEB, in general, 2 m surface temperatures in summer over urban areas are generally expected to continue rising sharply, particularly under the RCP8.5 scenario, where temperatures are projected to be approximately 8 °C higher by the end of the 21st century compared to the current climate. In the RCP4.5-based projections, despite a slower rate of increase than in RCP8.5, temperatures are expected to continue rising until 2060. However, from the 2060s onwards, large inter-decadal variation is anticipated without a continuous warming trend, resulting in temperatures about 3 °C higher at the end of the 21st century than in the current climate. Conversely, for precipitation, no clear long-term trends are found, unlike for 2 m surface temperature, although large interannual variability is expected. Interestingly, the mean value for future precipitation under the RCP8.5 scenario is expected to be overall lower by around 0.3 mm/day than that of the current climate.

Examining the time series of the simulated deviations of GEM_TEB relative to GEM for 2 m surface temperature, the summer mean UHI intensity is projected to steadily diminish (by approximately 0.10 °C) until the end of the 21st century, which is primarily associated with a noticeable weakening (about 0.15 °C) of Urban Heat Island (UHI) intensity during nighttime. In daily maximum temperature based on the RCP8.5 scenario, the weakening (about 0.09 °C) of Urban Heat Island (UHI) intensity is noticeably found by 2030 but after that inter-decadal variability with no additional weakening trend is expected, which seems to be related to urban-related precipitation variations. For the RCP4.5 scenario, the weakening (about 0.06 °C) of Urban Heat Island (UHI) intensity during nighttime is also found by 2050, similarly to the RCP8.5 scenario, but after that, there is no weakening trend. This seems to coincide with the time when RCP4.5-based GEM_TEB simulated temperature rise stops and stabilizes (Figure 5a). For daily maximum temperature based on the RCP4.5 scenario, weakening trend of Urban Heat Island (UHI) intensity by 2030 is similar to RCP8.5 but Urban Heat Island (UHI) intensity is dramatically restored between 2030 and 2035 to values similar to the current climate and even strengthens by around 0.06 °C between 2035 and 2045 compared to the current climate. These opposite results between 2035 and 2045 according to RCP scenarios can be explained by the spatial pattern of the precipitation difference for this period. That is, as shown in Figure 6, for the RCP4.5 scenario, the 2035–2045 minus 1981–2010 summer climatology of GEM_TEB minus GEM-simulated precipitation is relatively small for urban areas, which are well-matched with the higher daily maximum temperature. Therefore, this indicates that the different precipitation variations depending on RCP scenarios—specifically the stabilization of warming in RCP4.5 versus the sustained warming and altered hydrologic cycle in RCP8.5—subsequently affect urban–climate interactions. In the high-emission RCP8.5 scenario, the intensified urban-induced convective precipitation leads to a more robust increase in the evaporative fraction, resulting in a more pronounced weakening of the summer mean UHI compared to the RCP4.5 scenario. Interestingly, the variability in urban-induced precipitation difference is expected to grow further after 2060, which seems to largely affect fluctuation in urban-induced daily maximum temperature.

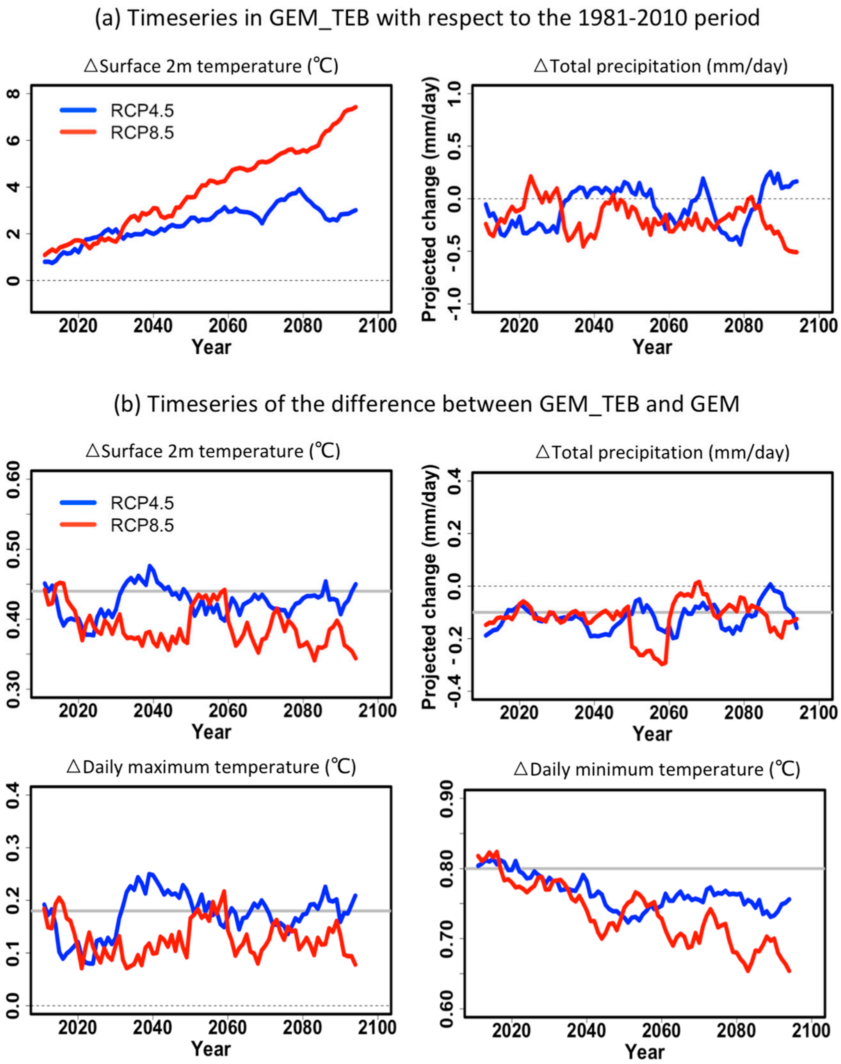

Figure 5. (**a**) Projected changes in 2 m surface temperature (°C) and precipitation (mm/day) simulated by GEM_TEB driven by CanESM2 according to RCP scenarios with respect to the 1981–2010 period over all urban regions. The 10-year moving average of summer means is shown to highlight long-term trends. (**b**) Timeseries of differences between projected changes to 2 m surface temperature (°C), total precipitation (mm/day), and daily maximum and minimum temperatures (°C) simulated by two experiments (GEM_TEB minus GEM) are also shown. Raw values are presented here to illustrate the full, continuous spectrum of variability; values near zero inherently indicate a lack of statistically significant urban-induced impact. The gray solid line in each sub-figure indicates the mean value of the difference between the two experiments for the 1981–2010 period.

Figures 7 and 8 show the projected changes to the spatial distribution of summer mean 2 m surface temperature (°C) and precipitation (mm/day) simulated by GEM_TEB driven by CanESM2 for the future climate (2071–2100) based on the RCP4.5 and 8.5 scenarios, respectively, compared to the current climate (1981–2010). The differences between future and current climates simulated by GEM_TEB minus GEM for daily maximum and minimum temperatures, evaporative fraction (defined as the ratio of latent heat flux to the sum of latent and sensible heat fluxes), and precipitation are also presented to investigate the causes of changes in urban–climate interactions. Overall, GEM_TEB projects summer temperature increases over the entire analysis domain for the future climate, with relatively higher increases for high-latitude regions and under the RCP8.5 scenario. The area-averaged temperature increase is about 3.28 °C in RCP4.5 and 6.43 °C in RCP8.5. For precipitation changes in both RCP scenarios, opposing trends depending on climatological regions are expected. Specifically, precipitation is projected to increase by around 0.5–1.0 mm/day for coastal regions but precipitation decreases by around 0.5–1.0 mm/day for Great Lakes and inland regions are projected, which, as a result, lead to minimal net changes in the domain average (−0.10 to −0.25 mm/day) due to the offsetting effects between coastal increases and inland decreases. However, these regional disparities are statistically significant at the grid level and play a critical role in driving localized urban–climate feedback mechanisms. The contrasting precipitation responses—whereby coastal increases are largely offset by inland decreases, resulting in a minimal net regional change—are fundamentally governed by spatially distinct thermodynamic mechanisms. In coastal regions, the amplified land–sea thermal contrast under warming conditions intensifies local convergence and convective activity, which is effectively sustained by an abundant marine moisture supply. Conversely, inland regions experience pronounced boundary-layer drying driven by elevated temperatures and increased vapor pressure deficits (VPD), which severely restrict moisture availability for precipitation. Consequently, the relatively small net change in precipitation at the regional scale reflects a competing influence between moisture-enhanced convection near the coasts and moisture-limited suppression inland. These spatially coherent thermodynamic patterns provide a robust physical framework for understanding the near-zero net precipitation change across the broader domain, highlighting the critical role of proximity to continuous moisture sources in modulating urban–climate feedbacks.

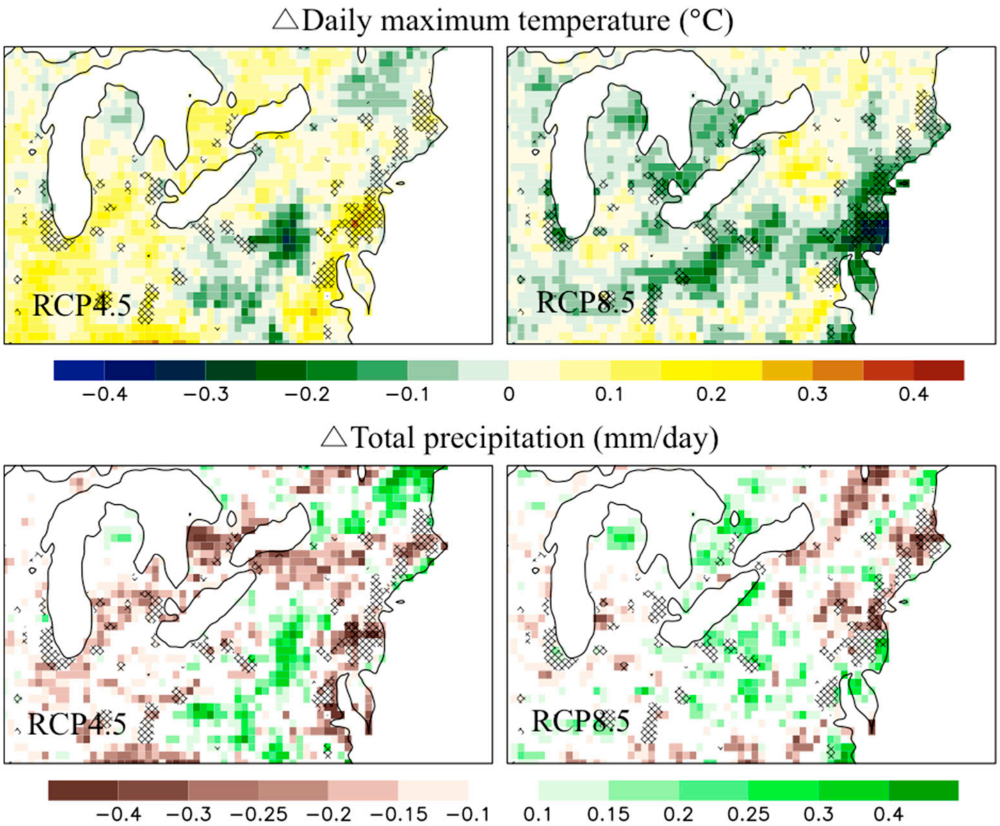

Figure 6. The 2035–2045 minus 1981–2010 summer climatology of GEM_TEB minus GEM-simulated daily maximum temperature and total precipitation, driven by CanESM2 based on RCP4.5 and 8.5 scenarios. In these spatial maps, only grid cells with changes significant at the 5% level ($p < 0.05$) based on a Student's *t*-test are color-shaded, while non-significant values are left blank to highlight robust anomalies. This specific decadal window highlights the anomalous strengthening of the daytime Urban Heat Island (UHI) intensity observed strictly under the RCP4.5 scenario.

https://doi.org/10.3390/atmos17050441

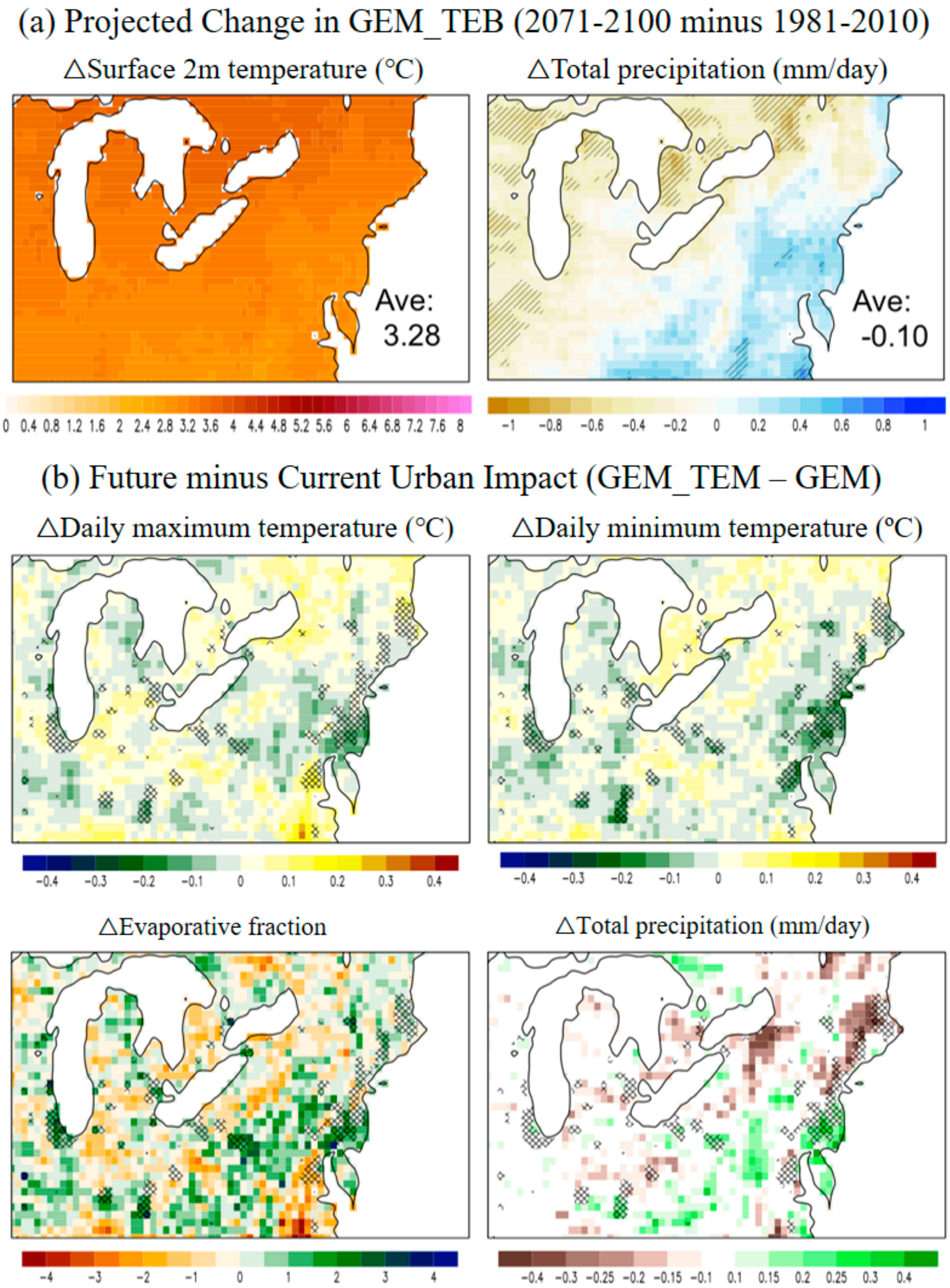

Figure 7. Comparative grid for the RCP4.5 scenario illustrating: (**a**) absolute projected changes (2071–2100 minus 1981–2010) and (**b**) the shift in urban impacts, calculated as [Future (GEM_TEB minus GEM)] minus [Current (GEM_TEB minus GEM)] to isolate the thermodynamic evolution of urban feedbacks. The evaporative fraction is defined as the ratio of latent heat flux to total surface heat flux. Regarding statistical transparency, hatching in (**a**) indicates 5% significance, while in (**b**), only significant differences ($p < 0.05$) are color-shaded. Hatched areas in (**b**) denote urban regions, and all temperature changes in (**a**) are statistically significant.

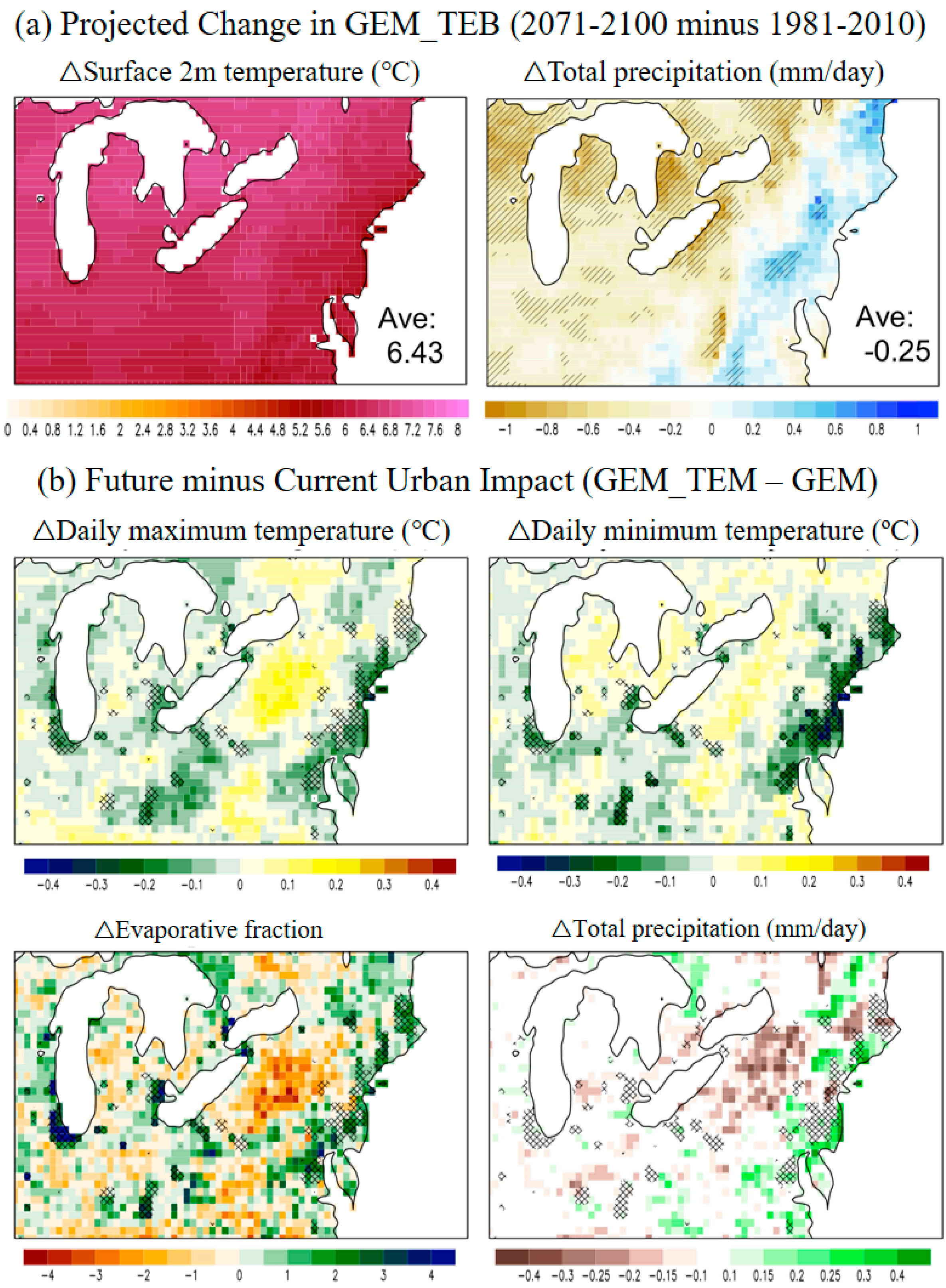

Figure 8. As in Figure 7, but for the RCP8.5 scenario: (**a**) absolute projected changes (2071–2100 minus 1981–2010) and (**b**) the shift in urban impacts based on the double-differencing formulation described previously. Statistical reporting follows the same criteria: hatching in (**a**) and color-shading in (**b**) denote 5% significance ($p < 0.05$). Hatched areas in (**b**) indicate urban regions, and surface air temperature changes in (**a**) are all statistically significant.

Regarding the changes in urban–climate interactions in the future climate (2071–2100) against the current climate (1981–2010), a noticeable weakening of Urban Heat Island (UHI) intensity during daytime and nighttime is found for urban grids, particularly for the RCP8.5 scenario. Interestingly, a stronger weakening of Urban Heat Island (UHI) intensity is well collocated with the regions exhibiting higher values of evaporative fraction, which is affected by urban-induced precipitation increases. In future precipitation changes as shown in Figures 7a and 8a, coastal areas in GEM_TEB are expected to experience precipitation increases for the future climate compared to the current climate, which leads to increased soil moisture in this area. Interestingly, even though it depends on the sub-coastal region and RCP scenarios, the urban-induced precipitation increases to total precipitation increases for coastal regions in the late 21st century contribute to about 20–40%. Oh and Sushama [2] reported that Urban Heat Island (UHI) intensity for coastal urban regions can lead to enhanced thermal (by convective available potential energy) and dynamic (by enhanced sea breeze with lower sea level pressure) convective developments, leading to higher precipitation for this region. These contrasting precipitation responses between coastal and inland regions are fundamentally linked to differences in regional moisture availability and dynamic circulation mechanisms. In coastal regions, urban-induced warming amplifies the land–sea thermal contrast, which strengthens the local pressure gradient and intensifies sea-breeze circulations. This enhanced dynamic forcing, combined with the proximity to a continuous marine moisture source, effectively promotes low-level moisture convergence and triggers convective precipitation over urbanized coastal areas. Consequently, these combined thermodynamic and dynamic effects drive the relatively larger urban-induced precipitation increases (accounting for 20–40% of the total increases) observed in coastal zones. Conversely, inland regions lack access to such a sustained external moisture source. In these areas, urban-induced warming primarily elevates surface temperatures and the vapor pressure deficit (VPD), which exacerbates boundary-layer drying and restricts moisture availability. As a result, the enhanced sensible heating in inland environments does not efficiently translate into increased convective precipitation, highlighting the critical role of background moisture and circulation regimes in modulating urban–climate interactions. It is, however, necessary to investigate the physical mechanisms driving the higher values of evaporative fraction in urban grid cells across the Great Lakes and inland regions in the future climate scenarios, despite the negligible differences between future and current precipitation projected by GEM_TEB minus GEM experiments. One possibility is that urban surfaces possess limited water retention capacity and low water-use efficiency [8,24,25]. In the TEB parameterization, urban surfaces are characterized by high imperviousness and minimal subsurface water storage. Consequently, intercepted precipitation is primarily retained in shallow surface reservoirs, such as roofs and pavements [24,25]. Under the significantly elevated temperatures and increased vapor pressure deficits projected in the RCP8.5 scenario, the atmospheric demand for moisture intensifies. As a result, water retained in these shallow urban depressions evaporates relatively quickly following localized precipitation events. This efficient removal of intercepted water via enhanced latent heat flux contributes to the overall summer mean increase in the urban evaporative fraction, contrasting with the more regulated, deeper soil–moisture-dependent transpiration processes over natural vegetative surfaces in the GEM experiment. Future research incorporating a multi-model ensemble and dynamic urban expansion scenarios would be beneficial to further quantify the uncertainties associated with GCM biases and land-use transitions.

We additionally analyze the correlation matrix for the relationships between changes in each surface variable based on the RCP8.5 scenario (Figure 9). In general, the changes in urban-induced daily maximum temperature warming show strongly negative correlations with changes in urban-induced evaporative fraction depending on the climatological regions. This suggests that the higher evaporative fraction (EF) in urban grid cells in the future climate is a key driver in weakening urban-induced daily maximum temperature warming. This phenomenon is particularly evident in coastal regions where urban-induced precipitation increases (contributing 20–40% to the total increase) enhance surface moisture availability. While a formal moisture budget decomposition—distinguishing local evaporation from moisture advection and separating convective from large-scale precipitation—is not explicitly performed, the spatial and thermodynamic patterns strongly suggest that the precipitation enhancement is primarily driven by local convective processes. Specifically, the localized increase in precipitation along coastal urban regions spatially coincides with an enhanced evaporative fraction and a concurrent reduction in sensible heat fluxes. This spatial coherence aligns with established physical mechanisms wherein urban-induced warming amplifies the land–sea thermal gradient, thereby intensifying sea-breeze circulations and promoting low-level moisture convergence over the aerodynamically rough urban canopy [40]. Consequently, the observed relationships in this study represent more than mere statistical correlations; they delineate a coherent thermodynamic and dynamical framework. Within this framework, enhanced coastal precipitation supplies the requisite surface moisture to sustain higher evaporative fractions, which in turn drives the projected UHI weakening. Future diagnostic studies incorporating full moisture budget assessments will be highly valuable to quantitatively partition these specific causal pathways. Furthermore, in a warmer climate, the immediate evaporation of limited captured water on impervious surfaces may also contribute to this transient cooling effect compared to the current climate. This phenomenon is more pronounced in the Great Lakes and inland regions than in coastal areas. Interestingly, inland regions show a higher positive correlation between urban-induced daily maximum temperature and downward longwave radiation than other sub-regions, which means that the inland regions are more susceptible to localized thermal trapping within urban canyons. Unlike coastal regions where sea breezes provide a ventilating effect, the relative stagnation of air in inland cities intensifies the sensitivity of surface temperature to downward longwave radiation emitted from urban facets. On the other hand, changes in urban-induced daily minimum temperature show highly positive correlations with changes in urban-induced daily maximum temperature compared to the other surface variables. The robust positive correlation between TMAX and TMIN changes (Figure 9) further confirms that the daytime evaporative cooling effect directly moderates the subsequent nighttime warming. In addition, unlike other sub-regions, positive relations between urban-induced surface wind speed and other surface variables are larger for coastal regions compared to the other sub-regions, which indicates strong dynamic feedback where urban-induced warming enhances the thermal gradient between land and sea, potentially intensifying sea breeze circulation. Specifically, the projected future warming over coastal urban areas strengthens the land–sea thermal contrast, which accelerates the sea breeze and leads to enhanced moisture convergence, further contributing to the localized precipitation increases observed in GEM_TEB. This intensified circulation subsequently influences urban–climate interactions by modifying moisture transport and convective development, as evidenced by the high positive correlations between wind speed and other surface variables unique to the coastal region. Although explicit quantification of high-frequency sea-breeze metrics—such as diurnal intensity and occurrence frequency—is not performed, a convergence of multiple lines of diagnostic evidence strongly supports the intensification of sea-breeze-like circulations under future warming. Specifically, the amplified land–sea thermal contrast, the spatial localization of precipitation increases predominantly along coastal regions, and their robust thermodynamic associations with surface wind speed anomalies (Figure 9) collectively indicate a strengthening of onshore flow and low-level moisture convergence. Therefore, rather than

https://doi.org/10.3390/atmos17050441

relying solely on direct circulation metrics, these coherent thermodynamic and dynamic diagnostics provide a physically robust framework demonstrating the amplification of coastal local circulations by urban-induced warming. Future investigations incorporating high-resolution diurnal wind profiling will be highly valuable to explicitly quantify these regional circulation changes.

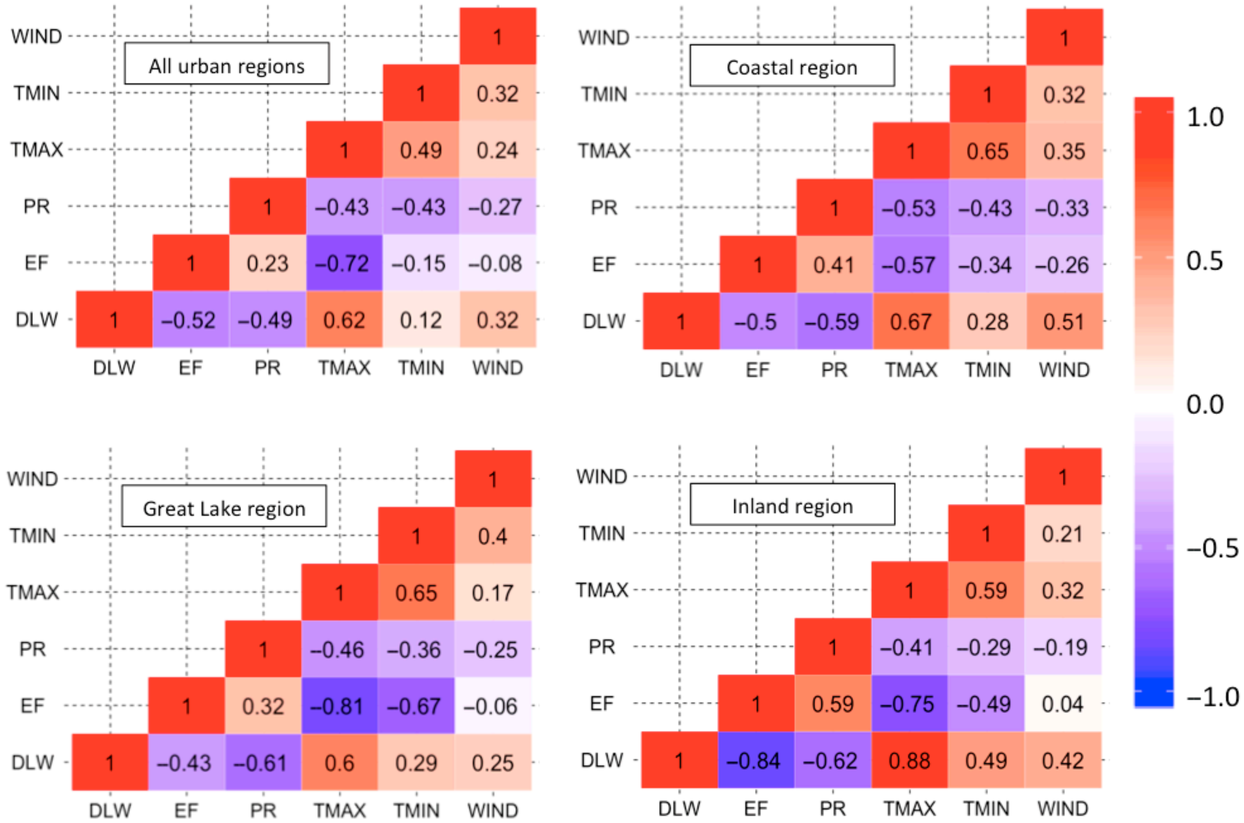

Figure 9. Correlation matrix of differences between projected changes for each variable derived from the difference between the two experiments (GEM_TEB minus GEM) for the future climate (2071–2100) based on the RCP8.5 scenario and compared to the current climate (1981–2010). The full matrix is presented to illustrate the continuous range of inter-variable relationships; correlation coefficients (R) approaching zero inherently signify a lack of statistical significance and a weak physical connection. The EF, DLW, PR, TMAX, TMIN, and WIND indicate the evaporation fraction, surface download longwave radiation, precipitation, daily maximum and minimum 2 m temperatures, and 10 m surface wind speed, respectively.

4. Summary and Conclusions

This study assesses projected changes to summertime urban–climate interactions over eastern North America using regional climate simulations at a 0.22° resolution for the 1981–2100 period under the RCP4.5 and RCP8.5 scenarios. To isolate urban impacts, two distinct experimental configurations were utilized: GEM_TEB, which incorporates the Town Energy Balance (TEB) scheme, and GEM, which does not. To account for the influence of boundary forcing quality on model performance, results were compared against prior simulations driven by the ERA-Interim reanalysis. Furthermore, the study investigates the role of geographic location by analyzing three climatologically distinct sub-regions: coastal, Great Lakes, and inland regions.

For the current climate period (1981–2010), the GEM_TEB experiments reasonably reproduce the observed spatial distributions of summer mean 2 m surface temperature and precipitation. While the baseline simulations driven by CanESM2 exhibit systematic warm (3.05 °C) and dry (1.19 mm/day) biases inherited from the parent global model, this study mitigates the impact of these absolute biases by employing a paired-difference framework (GEM_TEB minus GEM). Because both experiments share identical boundary conditions, this methodological approach inherently suppresses the influence of shared large-scale circulation errors, thereby allowing for a rigorous isolation of the urban-induced signals [2,13]. Previous regional climate modeling studies confirm that simulated land-surface and urban signals remain largely preserved under such paired configurations, even in the presence of systematic mean-state biases [41–43]. Consequently, the projected relative changes provide a scientifically credible basis for evaluating future urban–climate interactions. Through this approach, the GEM_TEB framework demonstrates significant added value via dynamic downscaling. Specifically, GEM_TEB isolates localized urban signals, simulating urban temperatures 0.5–0.7 °C higher and precipitation 0.2–0.4 mm/day lower than the GEM experiment. These refined simulations, primarily driven by urban-induced modifications to the surface energy balance, contribute to overall model improvement when validated against observations.

In the future climate (2011–2100), the Urban Heat Island (UHI) intensity for summer mean 2 m surface temperature is projected to weaken steadily by approximately 0.10 °C by the end of the 21st century. This trend is most prominent under the RCP8.5 scenario and is largely attributed to a significant weakening of the nighttime UHI by approximately 0.15 °C. An analysis of daily maximum temperatures under RCP8.5 reveals a noticeable UHI weakening of 0.09 °C by 2030; however, the subsequent period is characterized by inter-decadal variability without a clear weakening trend, a phenomenon likely linked to variations in urban-induced precipitation. These findings align with previous research suggesting a future weakening of UHI intensity, though this study identifies more pronounced weakening trends in daily minimum temperatures than in maximum temperatures, especially in coastal regions. Correlation matrix analysis further elucidates the physical mechanisms, showing that the weakening of daytime UHI intensity is negatively correlated with higher values of the urban-induced evaporative fraction. This increase in evaporative cooling is partly explained by urban-induced precipitation rises, particularly in coastal urban regions. Moreover, the mitigation of daytime warming is found to be largely responsible for the subsequent weakening of daily minimum temperature warming. The study also highlights that future regional climate in coastal urban areas will be more significantly impacted by changes in surface wind speed compared to other sub-regions. Consequently, this research demonstrates that the evolution of urban–climate interactions in a warming climate is highly dependent on regional climatological characteristics, providing a critical foundation for future investigations into urban impacts on short-duration precipitation extremes.

While the reliance on a single driving GCM (CanESM2) inherently limits the quantification of structural uncertainty, it is crucial to distinguish between the robustness of the underlying physical mechanisms and the certainty of their exact projected magnitudes. Although the precise quantitative magnitude of future urban impacts may exhibit sensitivity to the choice of the parent global model, the relative urban-induced thermodynamic responses and the identified feedback mechanisms remain highly robust. This physical robustness is fundamentally ensured by the paired experimental design (GEM_TEB versus GEM), which isolates the parameterized urban signal under consistent large-scale boundary conditions. Furthermore, the spatial coherence of these urban signals with those derived from independent ERA-Interim-driven simulations [2] confirms that the mechanistic pathways are not merely artifacts of the specific CanESM2 forcing. Consequently, the findings presented herein establish a critical, process-oriented baseline for understanding urban–climate interactions over eastern North America. Future research incorporating multi-model ensembles will be essential to comprehensively quantify the structural uncertainties associated with the exact magnitudes of these projected changes.

In addition to the large-scale forcing constraints, this study employs static urban parameters—such as urban fractions, building heights, and canyon aspect ratios—throughout the 1981–2100 simulation period. This experimental design is intentionally adopted to isolate the thermodynamic sensitivity of the existing urban fabric to greenhouse gas-induced warming. While urban morphologies inherently evolve over multi-decadal timescales, incorporating future urban expansion and morphological changes introduces substantial confounding uncertainties, as reliable long-term projections of land-use transitions remain highly scenario-dependent [26,44,45]. Consequently, utilizing a static urban representation provides a rigorously controlled experimental framework for assessing climate-driven urban responses, consistent with established regional climate modeling practices. It is recognized that future urban expansion and densification could enhance sensible heat fluxes, potentially offsetting a portion of the projected 0.10 °C summer mean UHI weakening. However, robustly quantifying this dynamic morphological effect requires speculative assumptions regarding future urban development pathways, which fall beyond the scope of this study. Therefore, the results presented herein establish a critical baseline thermodynamic response under a fixed urban morphology, serving as an essential reference for future coupled climate–urbanization assessments.

Importantly, the projected attenuation of daytime UHI intensity does not necessarily imply a reduction in overall urban heat hazards. The findings suggest that this relative daytime cooling is coupled with an enhanced evaporative fraction, which inherently increases 2 m surface atmospheric moisture. Because elevated humidity can exacerbate physiological heat stress, evaluating future urban thermal environments solely based on dry-bulb temperature metrics may not fully capture the actual human health risks. Therefore, to comprehensively assess the compounded risks of concurrent heat and humidity extremes in a warming climate, future investigations would benefit from incorporating integrated thermal comfort indices, such as the Wet-Bulb Globe Temperature (WBGT) (e.g., [26,44]).

Author Contributions: Conceptualization, J.K. and S.-G.O.; methodology, J.K.; software, J.K.; validation, J.K. and S.-G.O.; formal analysis, J.K.; investigation, J.K.; resources, S.-G.O.; data curation, J.K.; writing—original draft preparation, J.K.; writing—review and editing, S.-G.O.; supervision, S.-G.O.; funding acquisition, S.-G.O. All authors have read and agreed to the published version of the manuscript.

Funding: This research received no external funding.

Institutional Review Board Statement: Not applicable.

Informed Consent Statement: Not applicable.

Data Availability Statement: The GEM simulations driven by CanESM2 used in this study are extensive in size. Therefore, the dataset cannot be made publicly available at this time, but can be provided upon reasonable request. Interested researchers are encouraged to contact the corresponding author for access.

Acknowledgments: The GEM simulations considered in this study were performed on the supercomputer managed by Compute Canada and Calcul Québec.

Conflicts of Interest: The authors declare no conflict of interest.

References

1. Daniel, M.; Lemonsu, A.; Déqué, M.; Somot, S.; Alias, A.; Masson, V. Benefits of explicit urban parameterization in regional climate modeling to study climate and city interactions. *Clim. Dyn.* **2019**, *52*, 2745–2764. [CrossRef]
2. Oh, S.-G.; Sushama, L. Urban-climate interactions during summer over eastern North America. *Clim. Dyn.* **2021**, *57*, 3015–3028. [CrossRef]
3. Oke, T.R. The energetic basis of the urban heat island. *Q. J. R. Meteorol. Soc.* **1982**, *108*, 1–24. [CrossRef]

4. Wang, D.; Jiang, P.; Wang, G.; Wang, D. Urban extent enhances extreme precipitation over the Pearl River Delta, China. *Atmos. Sci. Lett.* **2015**, *16*, 310–317. [CrossRef]
5. United Nations, Department of Economic and Social Affairs, Population Division. *World Population Prospects: The 2017 Revision, Key Findings and Advance Tables*; United Nations: New York, NY, USA, 2017; p. 47. Available online: https://population.un.org/wpp/Publications/Files/WPP2017_KeyFindings.pdf (accessed on 13 April 2026).
6. IPCC. Climate Change 2007: The Physical Science Basis. In *Contribution of Working Group I to the Fourth Assessment Report of the Intergovernmental Panel on Climate Change*; Solomon, S., Qin, D., Manning, M., Chen, Z., Marquis, M., Averyt, K.B., Tignor, M., Miller, H.L., Eds.; Cambridge University Press: Cambridge, UK; New York, NY, USA, 2007; p. 996. Available online: https://www.ipcc.ch/report/ar4/wg1/ (accessed on 13 April 2026).
7. McCarthy, M.P.; Best, M.J.; Betts, R.A. Climate change in cities due to global warming and urban effects. *Geophys. Res. Lett.* **2010**, *37*, L09705. [CrossRef]
8. Oleson, K.W. Contrasts between urban and rural climate in CCSM4 CMIP5 climate change scenarios. *J. Clim.* **2012**, *25*, 1390–1412. [CrossRef]
9. Oleson, K.W.; Bonan, G.B.; Feddema, J.; Jackson, T. An examination of urban heat island characteristics in a global climate model. *Int. J. Climatol.* **2011**, *31*, 1848–1865. [CrossRef]
10. Oh, S.G.; Park, J.-H.; Lee, S.-H.; Suh, M.-S. Assessment of the RegCM4 over East Asia and future precipitation change adapted to the RCP scenarios. *J. Geophys. Res. Atmos.* **2014**, *119*, 2913–2927. [CrossRef]
11. Oh, S.G.; Suh, M.S. Effects of irrigated cropland on the local and regional climate over Northeast Asia in a regional climate model. *Asia-Pac. J. Atmos. Sci.* **2019**, *55*, 351–371. [CrossRef]
12. Teufel, B.; Diro, G.T.; Whan, K.; Milrad, S.M.; Jeong, D.I.; Ganji, A.; Huziy, O.; Winger, K.; Gyakum, J.R.; de Elia, R.; et al. Investigation of the 2013 Alberta flood from weather and climate perspectives. *Clim. Dyn.* **2017**, *48*, 2881–2899. [CrossRef]
13. Bélair, S.; Leroyer, S.; Seino, N.; Spacek, L.; Souvanlasy, V.; Paquin-Ricard, D. Role and impact of the urban environment in a numerical forecast of an intense summertime precipitation event over Tokyo. *J. Meteorol. Soc. Jpn.* **2018**, *96A*, 77–94. [CrossRef]
14. Cote, J.; Gravel, S.; Methot, A.; Patoine, A.; Roch, M.; Staniforth, A. The operational CMC-MRB global environmental multiscale (GEM) model. Part I: Design considerations and formulation. *Mon. Weather Rev.* **1998**, *126*, 1373–1395. [CrossRef]
15. Yeh, K.S.; Cote, J.; Gravel, S.; Methot, A.; Patoine, A.; Roch, M.; Staniforth, A. The CMC-MRB global environmental multiscale (GEM) model. Part III: Nonhydrostatic formulation. *Mon. Weather Rev.* **2002**, *130*, 339–356. [CrossRef]
16. Kain, J.S.; Fritsch, J.M. The role of the convective "trigger function" in numerical forecasts of mesoscale convective system. *Meteorol. Atmos. Phys.* **1992**, *49*, 93–106. [CrossRef]
17. Bélair, S.; Mailhot, J.; Girard, C.; Vaillancourt, P. Boundary layer and shallow cumulus clouds in a medium-range forecast of a large-scale weather system. *Mon. Weather Rev.* **2005**, *133*, 1938–1960. [CrossRef]
18. Sundqvist, H.; Berge, E.; Kristjánsson, J.E. Condensation and cloud parameterization studies with a mesoscale numerical weather prediction model. *Mon. Weather Rev.* **1989**, *117*, 1641–1657. [CrossRef]
19. Li, J.; Barker, H.W. A radiation algorithm with correlated-k distribution. Part I: Local thermal equilibrium. *J. Atmos. Sci.* **2005**, *62*, 286–309. [CrossRef]
20. Benoit, R.; Cote, J.; Mailhot, J. Inclusion of a Tke boundary-layer parameterization in the Canadian regional finite-element model. *Mon. Weather Rev.* **1989**, *117*, 1726–1750.
21. Delage, Y. Parameterising sub-grid scale vertical transport in atmospheric models under statistically stable conditions. *Bound.-Layer Meteorol.* **1997**, *82*, 23–48. [CrossRef]
22. Zadra, A.; McTaggart-Cowan, R.; Roch, M. Recent Changes to the Orographic Blocking. In Proceedings of the Seminar Presentation at PRN, Dorval, QC, Canada, 30 March 2012. Available online: http://collaboration.cmc.ec.gc.ca/science/rpn/SEM/dossiers/2012/seminaires/2012-03-30/Seminar_2012-03-30_Ayrton-Zadra.pdf (accessed on 13 April 2026).
23. Verseghy, D.L. *CLASS—The Canadian Land Surface Scheme (Version 3.4)—Technical Documentation (Version 1.1)*; Internal Report; Climate Research Division, Science and Technology Branch, Environment Canada: Toronto, ON, Canada, 2009; p. 183. Available online: https://publications.gc.ca/ (accessed on 13 April 2026).
24. Masson, V. A physically-based scheme for the urban energy budget in atmospheric models. *Bound.-Layer Meteorol.* **2000**, *94*, 357–397. [CrossRef]
25. Masson, V.; Grimmond, C.S.B.; Oke, T.R. Evaluation of the town energy balance (TEB) scheme with direct measurements from dry districts in two cities. *J. Appl. Meteorol.* **2002**, *41*, 1011–1026. [CrossRef]
26. Oke, T.R. The urban energy balance. *Prog. Phys. Geogr.* **1988**, *12*, 471–508. [CrossRef]
27. Martynov, A.; Laprise, R.; Sushama, L.; Winger, K.; Separovic, L.; Dugas, B. Reanalysis-driven climate simulation over CORDEX North America domain using the Canadian regional climate model, version 5: Model performance evaluation. *Clim. Dyn.* **2013**, *41*, 2973–3005. [CrossRef]
28. Chikhar, K.; Gauthier, P. Impact of analyses on the dynamical balance of global and limited-area atmospheric models. *Q. J. R. Meteorol. Soc.* **2014**, *140*, 1400–1413. [CrossRef]

29. O'Neill, B.C.; Tebaldi, C.; van Vuuren, D.P.; Eyring, V.; Friedlingstein, P.; Hurtt, G.; Knutti, R.; Kriegler, E.; Lamarque, J.F.; Lowe, J.; et al. The Scenario Model Intercomparison Project (ScenarioMIP) for CMIP6. *Geosci. Model Dev.* **2016**, *9*, 3461–3482. [CrossRef]
30. Tebaldi, C.; Debeire, K.; Eyring, V.; Fischer, E.; Fyfe, J.; Friedlingstein, P.; Knutti, R.; Lowe, J.; O'Neill, B.; Sanderson, B.; et al. Climate model projections from the Scenario Model Intercomparison Project (ScenarioMIP) of CMIP6. *Earth Syst. Dyn.* **2021**, *12*, 253–293. [CrossRef]
31. Böhnisch, A.; Ludwig, R.; Leduc, M. Using a nested single-model large ensemble to assess the internal variability of the North Atlantic Oscillation and its climatic implications for central Europe. *Earth Syst. Dyn.* **2020**, *11*, 617–640. [CrossRef]
32. Arora, V.K.; Scinocca, J.F.; Boer, G.J.; Christian, J.R.; Denman, K.L.; Flato, G.M.; Kharin, V.V.; Lee, W.G.; Merryfield, W.J. Carbon emission limits required to satisfy future representative concentration pathways of greenhouse gases. *Geophys. Res. Lett.* **2011**, *38*, L05805. [CrossRef]
33. Marey, A.; Ghadi, A.; Elhenawy, Y. Urban climate simulation for extreme heat events—A comparison between WRF and GEM. *Urban Clim.* **2025**, *59*, 102570. [CrossRef]
34. Thornton, M.M.; Shrestha, R.; Wei, Y.; Thornton, P.E.; Kao, S.-C. *Daymet: Daily Surface Water Data on a 1 Km Grid for North America, Version 3*; ORNL DAAC: Oak Ridge, TN, USA, 2017. [CrossRef]
35. Dee, D.P.; Uppala, S.M.; Simmons, A.J.; Berrisford, P.; Poli, P.; Kobayashi, S.; Andrae, U.; Balmaseda, M.A.; Balsamo, G.; Bauer, P.; et al. The ERA-Interim reanalysis: Configuration and performance of the data assimilation system. *Q. J. R. Meteorol. Soc.* **2011**, *137*, 553–597. [CrossRef]
36. Taylor, E. Summarizing multiple aspects of model performance in a single diagram. *J. Geophys. Res. Atmos.* **2001**, *106*, 7183–7192. [CrossRef]
37. Imhoff, M.L.; Zhang, P.; Wolfe, R.E.; Bounoua, L. Remote sensing of the urban heat island effect across biomes in the continental USA. *Remote Sens. Environ.* **2010**, *114*, 504–513. [CrossRef]
38. Zhao, L.; Lee, X.; Smith, R.B.; Oleson, K. Strong contributions of local background climate to urban heat islands. *Nature* **2014**, *511*, 216–219. [CrossRef]
39. Wouters, H.; De Ridder, K.; Demuzere, M.; Lauwaet, D.; van Lipzig, N.P.M. The diurnal evolution of the urban heat island of Paris: A model-based case study during summer 2006. *Atmos. Chem. Phys.* **2013**, *13*, 8525–8541. [CrossRef]
40. Shepherd, J.M. A review of current investigations of urban-induced rainfall and recommendations for the future. *Earth Interact.* **2005**, *9*, 1–27. [CrossRef]
41. Christensen, J.H.; Boberg, F.; Christensen, O.B.; Lucas-Picher, P. On the need for bias correction of regional climate change projections of temperature and precipitation. *Geophys. Res. Lett.* **2008**, *35*, L20709. [CrossRef]
42. Hawkins, E.; Sutton, R. The potential to narrow uncertainty in regional climate predictions. *Bull. Am. Meteorol. Soc.* **2009**, *90*, 1095–1107. [CrossRef]
43. Hernández-Díaz, L.; Laprise, R.; Nikiéma, O.; Winger, K.; Dandoy, S. Effect of empirical correction of sea-surface temperature biases on the CRCM5-simulated climate and projected climate changes over North America. *Clim. Dyn.* **2019**, *53*, 453–476. [CrossRef]
44. Hamdi, R.; Kusaka, H.; Doan, Q.-V.; Cai, P.; He, H.; Luo, G.; Kuang, W.; Caluwaerts, S.; Duchêne, F.; Van Schaeybroek, B.; et al. The state-of-the-art of urban climate change modeling and observations. *Earth Syst. Environ.* **2020**, *4*, 631–646. [CrossRef]
45. Huszar, P.; Halenka, T.; Belda, M.; Zak, M.; Sindelarova, K.; Miksovsky, J. Regional climate model assessment of the urban land-surface forcing over central Europe. *Atmos. Chem. Phys.* **2014**, *14*, 12393–12413. [CrossRef]

https://doi.org/10.3390/atmos17050441